Broadband single-shot electron spectrometer for GeV-class laser-plasma-based accelerators

K. Nakamura,[a] W. Wan, N. Ybarrolaza, D. Syversrud, J. Wallig, and W. P. Leemans
Lawrence Berkeley National Laboratory, University of California, Berkeley, California 94720, USA

(Received 26 October 2007; accepted 25 April 2008; published online 20 May 2008)

Laser-plasma-based accelerators can provide electrons over a broad energy range and/or with large momentum spread. The electron beam energy distribution can be controlled via accurate control of laser and plasma properties, and beams with energies ranging from ≃0.5 to 1000 MeV have been observed. Measuring these energy distributions in a single shot requires the use of a diagnostic with large momentum acceptance and, ideally, sufficient resolution to accurately measure narrow energy spread beams. Such a broadband single-shot electron magnetic spectrometer for GeV-class laser-plasma-based accelerators has been developed at Lawrence Berkeley National Laboratory. Detailed descriptions of the design concept and hardware are presented, as well as a performance evaluation of the spectrometer. The spectrometer covered electron beam energies raging from 0.01 to 1.1 GeV in a single shot, and enabled the simultaneous measurement of the laser properties at the exit of the accelerator through the use of a sufficiently large pole gap. Based on measured field maps and third-order transport analysis, a few percent-level resolution and determination of the absolute energy were achieved over the entire energy range. Laser-plasma-based accelerator experiments demonstrated the capability of the spectrometer as a diagnostic and its suitability for measuring broadband electron sources. © *2008 American Institute of Physics.*
[DOI: 10.1063/1.2929672]

I. INTRODUCTION

A charged particle spectrometer[1] is one of the critical diagnostics for any particle accelerator.[2,3] Laser-driven wakefield accelerators (LWFAs) have shown significant progress over the past decade, and have attracted considerable interest as the next generation linear accelerators. For the present generation LWFAs, requirements placed on the electron spectrometer (ESM) are somewhat different from those for conventional accelerators. A broad momentum acceptance with high resolution is critical. LWFAs can operate in a regime where beams with large relative energy spread $\delta E/E$ are generated,[4–7] or, as has recently been shown, produce narrow ($<10\%$) $\delta E/E$ beams,[8–13] where E is the electron kinetic energy. In addition, by controlling laser and plasma conditions, it has been shown that narrow energy spread beams can be generated with energies ranging from 0.5 to 1 GeV.[14,15] To elucidate the mechanisms behinds those regimes hence requires the use of a ESM with broad momentum acceptance. Although the required momentum resolution for LWFA could be somewhat relaxed compared to those for conventional accelerators, it should perform at a few percent-level resolution to accurately measure the energy spread of the present generation LWFA beams.

Most spectrometer implementations use a dipole magnet as a dispersive element and a collimator to control the instrumental resolution. To detect the relativistic electron, a variety of detectors have been employed: surface barrier detectors,[4,5,16] cloud chambers,[16] thermoluminescent dosimeters,[17] scintillating fibers,[18,19] scintilators with photomultipliers,[6,7] imaging plates (IPs),[8,11,12,20] and scintillating screens, mostly Gadox ($Gd_2O_2S:Tb$) (Ref. 21) with films[4] or cameras (scintillator-camera).[6,13,15,16,22] IP and scintillator-camera detectors are now widely used for their capability of imaging, and hence, can provide detailed information about the spatial properties. Due to the capability for accumulative measurements, IP has an advantage in sensitivity, while scintillator-camera based system could allow a high repetition-rate operation.

Recently, production of up to 1 GeV electron beams (e-beams) via a capillary discharge guided (CDG)-LWFA has been demonstrated by the LOASIS Group at Lawrence Berkeley National Laboratory (LBNL).[14,15] When the CDG-LWFA experiments were designed, the decision was made to develop a magnet-based ESM with as large a momentum acceptance as possible and capable of measuring e-beam energies of order GeV. In the CDG-LWFA accelerator concept, guiding of an intense laser was critical for operation, therefore simultaneous measurement of laser output mode and e-beam properties was essential. In order to realize the simultaneous measurement, the laser beam had to be separated from the e-beam without significant distortion, and, to accommodate such a broad energy spectrum without having a large system, the ESM magnetic field had to be reasonably strong ($\geqslant 1$ T). In addition, the design needed to provide sufficient angular acceptance to address the e-beam angular properties, as well as single-shot evaluation capability with high repetition rate for statistical analysis. In this paper, the ESM design concept and the description of the hardware are

[a]Also at Nuclear Professional School, University of Tokyo, Tokai, Ibaraki 319-1188, Japan.

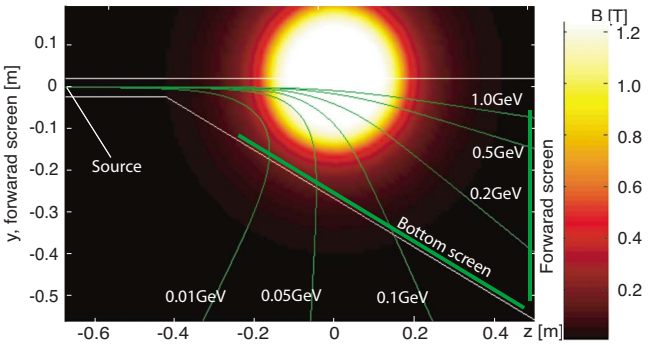

FIG. 1. (Color online) Electron trajectories (1.0, 0.5, 0.2, 0.1, 0.05, and 0.01 GeV) with a peak magnetic field of 1.25 T. The location of the scintillating screens and the vacuum chamber are also illustrated. The center of the magnet is at $z=0$. Shown by color map is the magnetic field profile. The source is the exit of the capillary discharge waveguide.

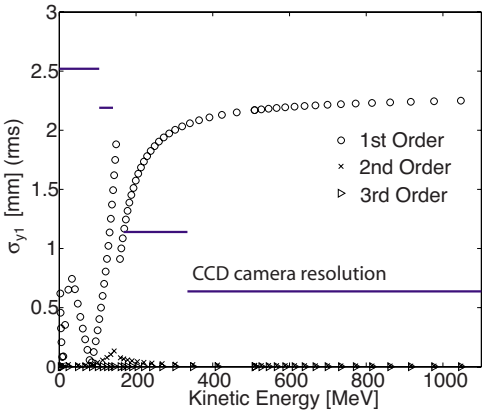

FIG. 2. (Color online) Calculated contributions to the vertical beam size of each order of the Taylor expansion of the electron beam orbit. The assumed input beam profile is a Gaussian distribution with $\sigma_{x0}=\sigma_{y0}=20$ μm (rms), and $\sigma_{x'0}=\sigma_{y'0}=2$ mrad (rms). The horizontal axis is the kinetic energy of the electron beam for a peak magnetic field of 1.25 T. Also shown by solid line is the spatial resolution of CCD cameras.

presented in Sec. II, followed by the performance evaluation of the ESM in Sec. III. Section IV presents experimental results, and a summary is given in Sec. V.

II. SPECTROMETER DESIGN

The electron spectrometer utilized a water-cooled round dipole electromagnet Varian 4012A, which had a 65 mm gap and was powered by a Glassman SH3R2.7 power supply. Since it was originally used for magnetic resonance experiments,[23] the field homogeneity in the flat region was very high ($<1\%$ variations). The magnetic field was measured by a Hall probe along the midplane,[1] and the effective radius, defined by $R_{\mathrm{eff}}=[\int_0^\infty B_x(r)dr]/B_x(0)$, was found to be 195 mm with peak field $B_x(0)=1.25$ T (see Fig. 1). The Hall probe was installed permanently to measure the peak magnetic filed strength $B_x(0)$ for each shot directly rather than deducing the peak field from the applied magnet current, which could lead to incorrect estimates due to the hysteresis. The magnet deflected the electrons vertically downward onto two scintillating screens (LANEX Fast Back from Kodak) mounted on the exit flanges of the vacuum chamber. Four synchronously triggered 12 bit charge-coupled device (CCD) cameras (model Flea from Point grey research) imaged a 75 cm long (bottom) and a 45 cm long (forward) screens, allowing simultaneous single-shot measurement of electrons from 0.01 to 0.14 GeV (bottom) and 0.17 to 1.1 GeV (forward) with a peak magnetic field of 1.25 T. Spatial resolutions of those CCD cameras were measured to be 0.6—1 mm for the forward screen and $\simeq$2.5 mm for the bottom screen (see Fig. 2). Stray laser light was blocked by $\simeq$40 μm thick aluminum foil on the back of the screens. In addition, bandpass filters (central wavelength of 550 nm, width of 70 nm full width half maximum) were installed in front of each CCD camera to separate green fluorescent light from the intense infrared laser light. To avoid electrons from hitting the CCD cameras directly, first-surface mirrors were used at 45° following the exit flanges, which separated fluorescent light from the electrons.

The total number of electrons was obtained from the intensity on the scintillating screen, which was cross-calibrated against an integrating current transformer (ICT) at the Advanced Light Source (ALS), LBNL.[24] By using an energy tunable (0.071–1.2 GeV), 20 ps long [root-mean-square, (rms)] electron beams, the intensity—number of electrons calibration was performed for an identical CCD camera and scintillating screen over a broad range of the electron energy. The sensitivity difference between the CCD cameras due to the different screen-camera distance was taken into account by using a LED source to cross-calibrate. Note that since the instantaneous intensity of the ALS e-beams [2.0 pC/ps mm^2 on the screen] was not as high as that of typical LWFAs, there is a possibility that the ALS calibration underestimated beam charge due to the saturation of the scintillating screen caused by the high instantaneous intensity of the e-beam. For example, a shot shown in Fig. 5(a) gave 23 pC/ps mm^2 on the screen where an e-beam was assumed to be 3.0 fs long (rms).[25] Therefore, in this paper, the estimated charge is presented as $>Q$ pC to be exact.

The requirements imposed on this design were (a) repetition rate of >1 Hz, (b) a few % level energy resolution and error in the determination of the absolute energy, (c) $>\pm 10$ mrad angular acceptance, and (d) system dimension as compact as $1\times1\times1$ m^3. The repetition rate of >1 Hz was achieved by using the scintillator-camera scheme. The imaging properties of the spectrometer were determined via the edge focusing. The displacement of the dipole magnet center with respect to the laser propagation axis was carefully chosen to provide the necessary edge focusing. One can achieve the minimum energy resolution and error in the determination of the absolute energy by observing e-beams at the foci in the dispersive plane.[26] By having the laser propagation axis below (above) the magnet center, the edges provide converging (diverging) power in the dispersive plane, and diverging (converging) power in the nondispersive plane. The stronger converging power in the dispersive plane provides a more compact system because the foci in the dispersive plane are closer to the magnet, while it results in a smaller angular acceptance due to the stronger diverging power in the nondispersive plane. High energy e-beams become somewhat insensitive to edge focusing due to their rigidity, and their resolutions are decided mostly by their

angular divergence. For observation of high energy e-beams, the forward view was arranged to achieve the desirable angular acceptance and system dimensions. The laser propagation axis was placed 25.4 mm below the magnet center to achieve desirable foci arrangement for the dispersive plane and reasonable angular acceptance (detailed in Sec. III). Note that the imaging (focusing) was achieved only in the dispersive plane. The bottom view was arranged (30° downward from the laser propagation axis) to observe e-beams as close to the calculated first-order foci in the dispersive plane as possible. A detailed evaluation of the resolution and acceptance as well as the definition of "order" are presented in Sec. III.

III. PERFORMANCE EVALUATION

The electron trajectories on the midplane (reference trajectories) were computed by calculating the deflection angle based on the Lorentz force. The input midplane field was generated through a two-dimensional interpolation of the measured field profile along the radial axis. The representative trajectories (1.0, 0.5, 0.2, 0.1, 0.05, and 0.01 GeV) under a peak magnetic field $B_x(0)=1.25$ T are shown in Fig. 1. Also shown is the magnetic field profile using a color map, and the locations of the screens. For each trajectory, the six-dimensional e-beam properties were calculated by using the arbitrary-order beam dynamics code COSY INFINITY (COSY).[27] To utilize the most accurate fringe field evaluation in COSY, the magnetic field profiles along each trajectory were fitted into a six parameter Enge function $F(s)$ of the form

$$F(s)=\frac{1}{1+\exp[a_1+a_2(s/D)+\ \ldots\ +a_6(s/D)^5]}, \tag{1}$$

where s is the distance to the effective field boundary along the central orbit of each trajectory, D is the gap of the magnet, and a_1-a_6 are the Enge coefficients. In COSY, a particle trajectory $\boldsymbol{X}(\boldsymbol{s})=(x,x',y,y',\delta l)$ is calculated in the form of a fivefold Taylor expansion, where x (y) indicates horizontal (vertical) plane, $x'=dx/ds$, $y'=dy/ds$, and δl is the path length difference from the reference trajectory. For example, an expansion is written for x as

$$x=\sum (x|x_0^{\kappa}y_0^{\lambda}x_0'^{\mu}y_0'^{\nu}\hat{p}^{\chi})x_0^{\kappa}y_0^{\lambda}x_0'^{\mu}y_0'^{\nu}\hat{p}^{\chi}. \tag{2}$$

Here, $\hat{p}=\delta p/p$ is a relative momentum spread, subscript 0 indicates that the quantity is evaluated at $s=0$, namely, at the e-beam source (see Fig. 1), and $(x|x_0^{\kappa}y_0^{\lambda}x_0'^{\mu}y_0'^{\nu}\hat{p}^{\chi})$ are the Taylor coefficients, which are functions of s. Note that for the fitting of the magnetic field profile, $s=0$ was defined at the effective boundary [see Eq. (1)]. The order of each term is given by the sum ord$=\kappa+\lambda+\mu+\nu+\chi$, and the order of the equation is given by the highest order among the terms. For example, a first-order equation for x can be written as

$$x|_{\text{first}}=(x|x_0)x_0+(x|y_0)y_0+(x|x_0')x_0'+(x|y_0')y_0' +(x|\hat{p}_0)\hat{p}_0. \tag{3}$$

Shown in Fig. 2 are the spatial resolutions of the CCD cameras and each order's contribution to vertical size σ_{y1} versus e-beam energy (assuming a zero energy spread), where σ is the rms width of the beam distribution and the subscript 1 indicates the output (at the screens). The peak magnetic field was 1.25 T, and the input beam profile was a Gaussian distribution with $\sigma_{x0}=\sigma_{y0}=20$ μm and $\sigma_{x'0}=\sigma_{y'0}=2$ mrad. The discontinuity at 160 MeV in Fig. 2 comes from the transition between different screens. One can see from Fig. 2 that the contribution from third-order effects is small. Therefore, calculations up to third-order give sufficient accuracy for the evaluation of the spectrometer performance. When the effective spatial resolution of the CCD camera is larger than the beam spot size, as in the low energy case, the momentum resolution would be limited by the CCD camera imaging (not the e-beam optics). Although the momentum resolution could be improved by an imaging system with higher spatial resolution, the scattering effect inside the screens[21] has to be addressed for a beam size below a few 100 μm.

Due to the collimator-free scheme, the measured momentum resolution contained a contribution from the e-beam divergence, which depended on the accelerator configuration and parameters such as the laser energy or the capillary length and diameter. As a result, the e-beam divergence showed shot-to-shot fluctuations. Therefore, the momentum resolution and the energy spread were evaluated for each shot with the following procedure. From the computed imaging properties, the horizontal beam divergence $\sigma_{x'0}$ was calculated from the measured horizontal beam size σ_{x1} with a given beam size at the source, σ_{x0} and σ_{y0}, which were assumed to be the same size as the laser output mode size. The effect of the source size on the image was almost negligible since the beam size at the source was smaller by an order of magnitude than the typical product of beam divergence and propagation distance. By assuming an axisymmetric electron beam profile (i.e., equal horizontal and vertical divergence), the vertical beam divergence $\sigma_{y'0}=\sigma_{x'0}$ was obtained and used to calculate the vertical beam size at the screen with a specific central energy and zero energy spread, $\sigma_{y1\text{mono}}$. The image size gave the intrinsic resolution of the ESM, δE_{mono}. The real energy spread of an electron beam δE_{beam} was then calculated by deconvolving the effect of finite divergence from the measured e-beam profile δE_{img} using $\delta E_{\text{img}}=\sqrt{\delta E_{\text{beam}}^2+\delta E_{\text{mono}}^2}$. The momentum resolutions for $\sigma_{x'0}=\sigma_{y'0}=1$ and 2 mrad electron beams are shown in Fig. 3, where the beam profile was assumed to be a Gaussian distribution with $\sigma_{x0}=\sigma_{y0}=20$ μm. The momentum resolution is below 2% (4%) for a 1 mrad (2 mrad) divergence beam in the energy range of the ESM. As discussed, and shown in Fig. 2, in the case where the beam size is smaller than the spatial resolution of the CCD cameras, the momentum resolution is limited by the CCD camera resolution, which can be seen in the region where the 1 and 2 mrad cases overlap.

The collimator-free scheme also introduced an uncertainty in the determination of the absolute energy.[15] The energy of an electron beam with positive (negative) incident angle in y (see Fig. 1 for coordinates) would be measured higher (lower) than the actual energy. The errors in the determination of the energy of electrons with certain incident angle (± 4 and ± 8 mrad) were computed and shown in Fig. 4, where the magnetic field was taken to be 1.25 T. For example, the electron beam measured as 1.0 GeV might have

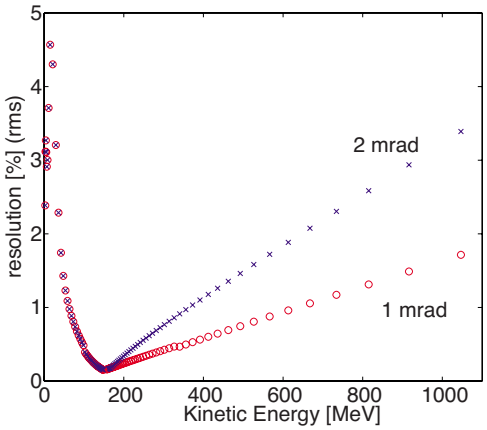

FIG. 3. (Color online) Momentum resolutions for $\sigma_{x'0}=\sigma_{y'0}=1$ and 2 mrad electron beams. Horizontal axis is the kinetic energy of the electron beam for a peak magnetic field of 1.25 T. The input beam size was assumed to be a Gaussian distribution with $\sigma_{x0}=\sigma_{y0}=20$ μm.

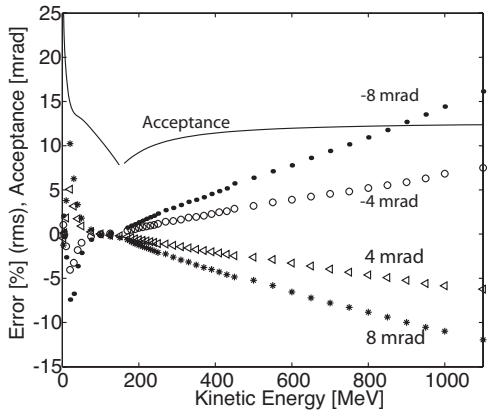

FIG. 4. Errors in the determination of the absolute energy for angles ranging from −8 to +8 mrad. Horizontal axis is the kinetic energy of the electron beam for a peak magnetic field of 1.25 T. The geometrical acceptance of the spectrometer is also shown (solid line).

been 0.94 (1.07) GeV with a 0.4 (−0.4) mrad incident angle. The fluctuation level in the incident angle in the vertical plane was evaluated as follows. From the measured beam position in the horizontal plane $x_{1\mathrm{peak}}$, the angular fluctuation in the horizontal plane $\sigma_{x1\mathrm{peak}}$ (rms) was statistically evaluated. With the assumption of symmetric behavior in both planes $\sigma_{y1\mathrm{peak}}=\sigma_{x1\mathrm{peak}}$, the fluctuations in the incident angle in the vertical plane were then determined. The angular fluctuations showed a dependence on the accelerator configuration (e.g., the laser energy or the capillary length and diameter), and the typical value was found to be 2 to 6 mrad (1σ), which gave ~3% to 11% error at 1.0 GeV, or ~1% to 5% error at 0.5 GeV. Also shown in Fig. 4 is the geometrical acceptance. The acceptance was trajectory dependent due to the differences in the path length and the imaging properties. More than ±10 mrad acceptance was achieved in most of the energy range.

IV. EXPERIMENTS

In this section, we present examples of single-shot beam measurements and analysis to demonstrate diagnostic performance. Experiments were performed by using a high peak power 10 Hz Ti:sapphire laser system of the LOASIS facility at LBNL and gas-filled capillary discharge waveguides developed at Oxford University.[14,15] The laser beam was focused onto the entrance of a capillary discharge waveguide by an $f/25$ off-axis parabolic mirror. A typical focal spot size was $w\simeq 25$ μm, which gave a calculated peak intensity $I\simeq 2P/\pi r_s^2\simeq 4\times 10^{18}$ W/cm^2 and a normalized vector potential $a_0\simeq 8.6\times 10^{-10}\lambda(\mu\mathrm{m})I^{1/2}(\mathrm{W/cm^2})\simeq 1.4$ with full energy and optimum compression (≃40 fs, 40 TW).

Shown in Fig. 5(a) is an example of a moderately resolved high energy e-beam. A 37 fs, 41 TW laser was focused onto a 33 mm long, 310 μm diameter capillary. The axial electron density[28] was $\simeq 4.3\times 10^{18}$ cm^{-3}, and the applied magnetic field was 1.25 T. A quasimonoenergetic beam with 778^{+44}_{-39} MeV peak energy and >3.3 pC total charge was observed. The beam divergence was found to be 2.5 mrad (1σ), which gave a resolution of 2.5% at 778 MeV. The energy spread was measured to be 4.6%. As stated in Sec.

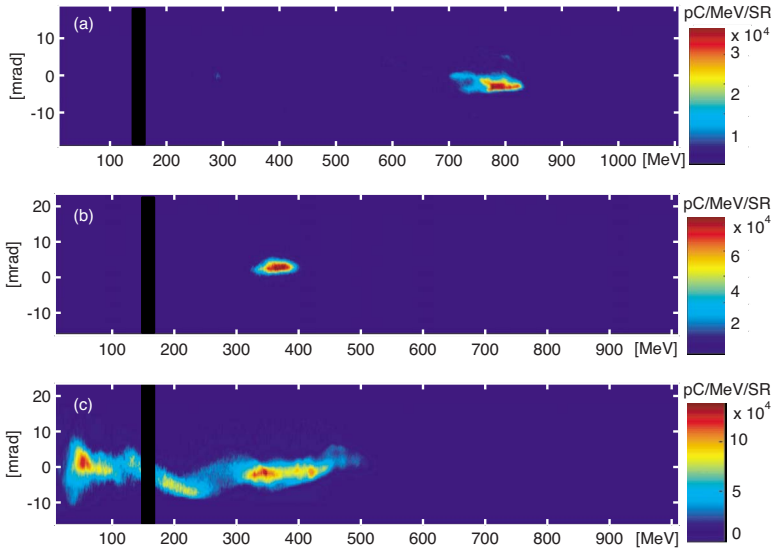

FIG. 5. (Color online) Single-shot spectra: (a) moderately resolved high energy e-beam, (b) finely resolved mono-energetic beam, and (c) finely resolved broadband beam. Horizontal axis is the kinetic energy of the electron beam for a peak magnetic field of (a) 1.25 T and [(b) and (c)] 1.14 T. Vertical axis is the electron beam angular divergence. Shown by a color map is the electron beam density in pC/MeV/str.

III, the estimated error range of the absolute energy value was computed from the beam angular fluctuation $\sigma_{x1\text{peak}}$, which was evaluated from 230 vicinity shots and found to be 4.6 mrad (1σ). Due to the nonlinearity in the space-energy relation, an estimated error of the absolute energy becomes asymmetric (see Fig. 4). In this paper, errors for $\pm 1\sigma_{x1\text{peak}}$ are presented.

Shown in Figs. 5(b) and 5(c) are examples of finely resolved quasimonoenergetic and broadband e-beams, respectively. The 33 mm long, 190 μm diameter capillary was used with a 46 fs, 15 TW laser in Fig. 5(b) and a 150 fs, 5 TW laser in Fig. 5(c). The axial electron densities were $\simeq 3.4 \times 10^{18}$ cm^{-3}, and the applied magnetic field was 1.14 T, which gave momentum acceptances from 0.009 to 1.0 GeV. A discussion on the dependence of the CDG-LWFA performance on laser-plasma parameters is beyond the scope of this paper, and the details of the laser-plasma interaction are presented in Ref. 15. A quasimonoenergetic beam with $364^{+7.6}_{-6.1}$ MeV peak energy and >3.3 pC total charge [Fig. 5(b)] and a broadband e-beam (from 10 to 450 MeV) with >42 pC total charge [Fig. 5(c)] were observed. For the quasi-monoenergetic beam [Fig. 5(b)], the beam divergence was found to be 1.3 mrad (1σ), which gave a resolution of 0.55% at 364 MeV. The energy spread was measured to be 5.0%. The beam angular fluctuation $\sigma_{x1\text{peak}}$ was evaluated from 360 vicinity shots and found to be 4.7 mrad (1σ). For the broadband beam [Fig. 5(c)], the divergence was $\simeq 2$ mrad (1σ) for the whole range, which gave less than 1% resolution for energies above 50 MeV (Fig. 3). Note that the simultaneous diagnoses of the laser output spots were successfully carried out for all measurements.[14,15]

V. SUMMARY

A broadband slitless, single-shot electron spectrometer for GeV-class laser-plasma-based accelerator beam measurements has been developed at the LOASIS facility of LBNL. A scintillator-camera based system was employed for relativistic e-beam detection for high repetition rate experiments. The spectrometer covered from 0.01 to 1.1 GeV in a single shot, with the ability of simultaneous measurement of e-beam spectra and output laser properties due to the absence of a slit. The design provided an unprecedented large momentum acceptance of a factor of 110 with reasonable resolution (below 5%). The design concept and hardware implementation were described, as well as the detailed analysis of the spectrometer performance. As shown in the Sec. IV, single-shot measurements with sufficient resolution and angular acceptance were demonstrated. The spectrometer design provides a powerful diagnostic tool for the research and development of the next generation LWFA.

ACKNOWLEDGMENTS

The authors acknowledge Gerry Dugan for contribution on the foci analysis, Bob Nagler and Michael Dickinson for implementation, Carl B. Schroeder, Anthony J. Gonsalves, Cameron G. R.Geddes, Estelle Cormier-Michel, Dmitriy Panasenko, Csaba Toth, and Eric Esarey for their contributions.

This work was supported by the Director, Office of Science, High Energy Physics, U.S. Department of Energy under Contract No. DE-AC02-05CH11231.

[1] K. L. Brown, Technical Report No. SLAC 75, 1975.
[2] T. Tajima and J. M. Dawson, Phys. Rev. Lett. **43**, 267 (1979).
[3] E. Esarey, P. Sprangle, J. Krall, and A. Ting, IEEE Trans. Plasma Sci. **24**, 252 (1996).
[4] A. Modena, Z. Najmudin, A. E. Dangor, C. E. Clayton, K. A. Marsh, C. Joshi, V. Malka, C. B. Darrow, C. Danson, D. Neely, and F. N. Walsh, Nature (London) **377**, 606 (1995).
[5] C. A. Coverdale, C. B. Darrow, C. D. Decker, W. B. Mori, K.-C. Tzeng, K. A. Marsh, C. E. Clayton, and C. Joshi, Phys. Rev. Lett. **74**, 4659 (1995).
[6] D. Umstadter, S.-Y. Chen, A. Maksimchuk, G. Mourou, and R. Wagner, Science **273**, 472 (1996).
[7] C. I. Moore, A. Ting, K. Krushelnick, E. Esarey, R. F. Hubbard, B. Hafizi, H. R. Burris, C. Manka, and P. Sprangle, Phys. Rev. Lett. **79**, 3909 (1997).
[8] S. Mangles, C. Murphy, Z. Najmudin, A. Thomas, J. Collier, A. Dangor, E. Divali, P. Foster, J. Gallacher, C. Hooker, D. Jaroszynski, A. Langley, W. Mori, P. Norreys, F. Tsung, R. Viskup, B. Walton, and K. Krushelnick, Nature (London) **431**, 535 (2004).
[9] C. G. R. Geddes, C. Tóth, J. van Tilborg, E. Esarey, C. B. Schroeder, D. Bruhwiler, C. Nieter, J. Cary, and W. P. Leemans, Nature (London) **431**, 538 (2004).
[10] J. Faure, Y. Glinec, A. Pukhov, S. Kiselev, S. Gordienko, E. Lefebvre, J.-P. Rousseau, F. Burgy, and V. Malka, Nature (London) **431**, 541 (2004).
[11] E. Miura, K. Koyama, S. Kato, N. Saito, M. Adachi, Y. Kawada, T. Nakamura, and M. Tanimoto, Appl. Phys. Lett. **86**, 251501 (2005).
[12] A. Yamazaki, H. Kotaki, I. Daito, M. Kando, S. V. Bulanov, T. Z. Esirkepov, S. Kondo, S. Kanazawa, T. Homma, K. Nakajima, Y. Oishi, T. Nayuki, T. Fujii, and K. Nemoto, Phys. Plasmas **12**, 093101 (2005).
[13] T. Hosokai, K. Kinoshita, T. Ohkubo, A. Maekawa, M. Uesaka, A. Zhidkov, A. Yamazaki, H. Kotaki, M. Kando, K. Nakajima, S. V. Bulanov, P. Tomassini, A. Giulietti, and D. Giulietti, Phys. Rev. E **73**, 036407 (2006).
[14] W. P. Leemans, B. Nagler, A. J. Gonsalves, C. Tóth, K. Nakamura, C. G. R. Geddes, E. Esarey, C. B. Schroeder, and S. M. Hooker, Nat. Phys. **2**, 696 (2006).
[15] K. Nakamura, B. Nagler, C. Tóth, C. G. R. Geddes, C. B. Schroeder, E. Esarey, W. P. Leemans, A. J. Gonsalves, and S. M. Hooker, Phys. Plasmas **14**, 056708 (2007).
[16] C. E. Clayton, M. J. Everett, A. Lal, D. Gordon, K. A. Marsh, and C. Joshi, Phys. Plasmas **1**, 1753 (1994).
[17] L. M. Chen, J. J. Park, K.-H. Hong, J. L. Kim, J. Zhang, and C. H. Nam, Phys. Rev. E **66**, 025402 (2002).
[18] C. Gahn, G. D. Tsakiris, K. J. Witte, P. Thirolf, and D. Habs, Rev. Sci. Instrum. **71**, 1642 (2000).
[19] H. Chen, P. K. Patel, D. F. Price, B. K. Young, P. T. Springer, R. Berry, R. Booth, C. Bruns, and D. Nelson, Rev. Sci. Instrum. **74**, 1551 (2003).
[20] K. A. Tanaka, T. Yabuuchi, T. Sato, R. Kodama, Y. Kitagawa, T. Takahashi, T. Ikeda, Y. Honda, and S. Okuda, Rev. Sci. Instrum. **76**, 013507 (2005).
[21] Rad-Icon Imaging Corp. (www.rad-icon.com), Scintillator options for shad-o-box cameras, Technical Report No. AN-07, Santa Clara, CA 95054, 2002.
[22] Y. Glinec, J. Faure, A. Guemnie-Tafo, V. Malka, H. Monard, J. P. Larbre, V. D. Waele, J. L. Marignier, and M. Mostafavi, Rev. Sci. Instrum. **77**, 103301 (2006).
[23] R. G. Schlecht and D. W. McColm, Phys. Rev. **142**, 11 (1966).
[24] K. Nakamura, "*Control of laser plasma based accelerators up to* 1 GeV," Ph.D. thesis, University of Tokyo, 2008.
[25] C. G. R. Geddes and E. Cormier-Michel, personal communication (2008).
[26] G. Dugan, A. Misuri, and W. Leemans, Design and performance estimates for the l'oasis experiment magnetic spectrometers, Technical Report No. LBNL-49394, Lawrence Berkeley National Laboratory, University of California, Berkeley, CA 94720, 2001.
[27] K. Makino and M. Berz, Nucl. Instrum. Methods Phys. Res. A **427**, 338 (1999).
[28] A. J. Gonsalves, T. P. Rowlands-Rees, B. H. P. Broks, J. J. A. M. van der Mullen, and S. M. Hooker, Phys. Rev. Lett. **98**, 025002 (2007).